GENERAL AND APPLIED PHYSICS

On the Use of Measured Post-Discharge Gas Temperature Profiles in the Kinetic Modeling of the Pink Afterglow of Flowing N₂ DC Discharges

J. Levaton[1] · A. N. Klein[1] · J. Amorim[2] · J. H. F. Severo[3]

Abstract

In this study, we investigate the significance of utilizing measured post-discharge gas temperature profiles versus employing a representative constant gas temperature value in the kinetic modeling of the pink afterglow (PA) generated by flowing nitrogen DC discharges. Both approaches have been employed in the literature for PA kinetic modeling studies yielding reliable results. However, until now, no work has explored the kinetics aspects associated to these different methodologies in PA modeling. Firstly, we measure the spatial gas temperature variation in the post-discharge region using optical emission spectroscopy (OES). These spatial profiles are then converted into temporal profiles. We derive representative constant gas temperature values by calculating the mean gas temperature from these profiles. Subsequently we utilize a well-stablished kinetic numerical model for the PA, which calculate the densities of 15 distinct electronic states of nitrogen molecules, including the $N_2(X\ ^1\Sigma_g^+,\ 0 \leq v \leq 45)$ vibrational states, as functions of the post-discharge residence time. We analyze the post-discharge density profiles of certain singlet and triplet molecular states as well as ions, considering the different gas temperature approximations. The excitation rates of these molecular states are also studied. The $N_2(X\ ^1\Sigma_g^+)$ vibrational distribution functions (VDF) are investigated. We have observed that the densities profiles and studied excitation rates are very similar for the two different assumptions, which validates the use of a representative constant gas temperature approximation in the absence of the measured temperature along the post-discharge. We observe global kinetic effects found for the different gas temperature approaches and it is demonstrated that these effects results from the VDFs behavior, which depends on the vibrational-vibrational (V-V) and vibrational-translational (V-T) rate constants that are functions of the gas temperature.

Keywords Nitrogen flowing post-discharge · Pink afterglow modeling · Post-discharge gas temperature profiles

1 Introduction

The nitrogen pink afterglow (PA) phenomenon, also referred to as short-lived afterglow (SLA) has been intensively studied in the last decades both experimentally [1–9] and theoretically [10–18]. The pink afterglow is a nitrogen plasma that is generated in the post-discharge region of flowing nitrogen discharges, encompassing direct current (DC), radio-frequency (RF), and microwave discharges. Phenomenologically, the pink afterglow is a pink color luminescence [19] that appears in the post-discharge tube downstream the discharge region, separated from that by a dark space zone, or a region with low intensity of light emission. The main nitrogen emission systems detected in the pink afterglow are the first positive, second positive and first negative systems [20], being the last one the signature of this phenomenon since it is generated by electronic transitions from molecular nitrogen ions that are generated by metastable atoms and molecules collisions in the post-discharge region. Moreover, the first negative system is responsible for the pink color typical of this regime of the nitrogen post-discharge. In the absence of the pink afterglow phenomenon the nitrogen post-discharge (early
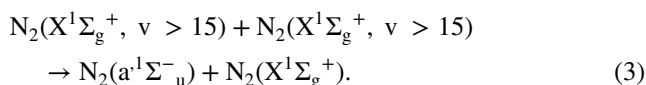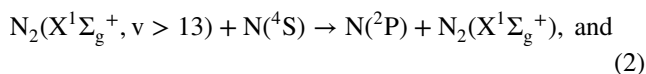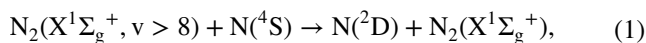
✉ J. Levaton
jacques.levaton@gmail.com

1 Laboratório de Materiais (LABMAT), Departamento de Engenharia Mecânica, Universidade Federal de Santa Catarina, Florianópolis, SC 88040-900, Brazil

2 Departamento de Física, Instituto de Ciências Exatas-ICEx, Universidade Federal Fluminense, Campus do Aterrado, Volta Redonda, RJ 27213-145, Brazil

3 Laboratório de Física de Plasmas, Instituto de Física, Universidade de São Paulo, São Paulo, SP 05508-090, Brazil

afterglow) presents predominant orange color. In this case we find the dominance of the second positive system (SPS) and first positive system (FPS) of the nitrogen molecules. When the pink afterglow occurs, the dominance of the first negative system (FNS), results in a post-discharge luminescence of pink color. The pink afterglow ionization mechanisms have been described in the literature from kinetic modeling mainly for nitrogen DC flowing discharges [9, 15, 17, 18] and microwave flowing discharges [10, 11, 13]. These mechanisms seem to take different physicochemical pathways in the DC and microwave discharges. The PA ionization mechanisms responsible for the production of $N_2^+(B^2\Sigma^+_u)$ electronically excited ions, which are responsible for the emissions of the first negative system in the post-discharge, follow a complex kinetic pathway in the DC discharge [15, 17, 18]. As the main phenomenon in this regime of the post-discharge, we find the relaxation process of the $N_2(X\,^1\Sigma^+_g)$ VDF with the post-discharge residence time. In this relaxation process, the VDF is populated in the intermediate and high vibrational levels due the V-V exchange reactions. These vibrational states initiate the ionization processes. Two groups of reactions generate the ionization. First, metastable atoms and molecules are formed by reactions involving the vibrational excited states of the fundamental electronic state of the nitrogen molecules $N_2(X^1\Sigma^+_g, v)$, as follows:

$$N_2(X^1\Sigma^+_g, v > 8) + N(^4S) \rightarrow N(^2D) + N_2(X^1\Sigma^+_g), \qquad (1)$$

$$N_2(X^1\Sigma^+_g, v > 13) + N(^4S) \rightarrow N(^2P) + N_2(X^1\Sigma^+_g), \text{ and} \qquad (2)$$

$$N_2(X^1\Sigma^+_g,\ v > 15) + N_2(X^1\Sigma^+_g,\ v > 15)$$
$$\rightarrow N_2(a'^1\Sigma^-_u) + N_2(X^1\Sigma^+_g). \qquad (3)$$

The $N(^4S)$ atoms are transported from the discharge region and also locally generated in the post-discharge region as detailed described in Ref. [16]. Additionally, $N(^2P)$ metastable atoms are also formed by the following reaction [21]:

$$N_2(A^3\Sigma^+_u) + N(^4S) \rightarrow N(^2P) + N_2(X^1\Sigma^+_g). \qquad (4)$$
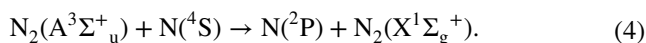
The formation of $N_2(A^3\Sigma^+_u)$ metastable in the post-discharge will be analyzed in the discussion section. Then, in a certain temporal range (0.1 – 2 ms) of the post-discharge residence times [16] the atoms associative ionization reaction is the dominant ionization channel [17, 18], as follows:
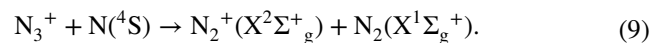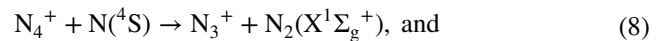
$$N(^2D) + N(^2P) \rightarrow N_2^+(X^2\Sigma^+_g) + e. \qquad (5)$$
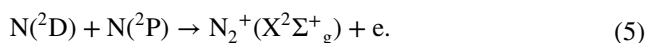
In another temporal range (2 – 100 ms), ionization occurs via reaction [15, 17, 18]:

$$N_2(a'^1\Sigma^-_u) + N_2(X^1\Sigma^+_g, v > 24) \rightarrow N_4^+ + e. \qquad (6)$$
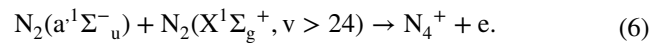
The $N_2^+(B^2\Sigma^+_u)$ excited ions are formed by the reaction:

$$N_2^+(X^2\Sigma^+_g) + N_2(X^1\Sigma^+_g, v > 11) \rightarrow N_2^+(B^2\Sigma^+_u) + N_2(X^1\Sigma^+_g). \qquad (7)$$
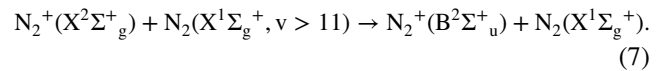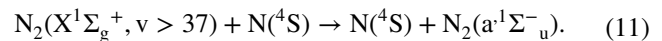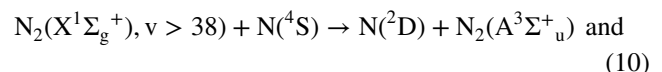
In the case of ions formed by reaction (6), there are additional ion converting mechanisms acting in the formation of $N_2^+(X^2\Sigma^+_g)$ ions before their excitation by reaction (7). These mechanisms are the reactions:

$$N_4^+ + N(^4S) \rightarrow N_3^+ + N_2(X^1\Sigma^+_g), \text{ and} \qquad (8)$$

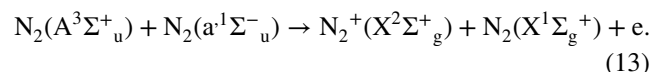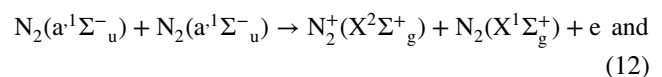$$N_3^+ + N(^4S) \rightarrow N_2^+(X^2\Sigma^+_g) + N_2(X^1\Sigma^+_g). \qquad (9)$$

In those cited works and in our present study, the pink afterglow is described as a non-equilibrium plasma, that is, ambipolar diffusion for ions and the condition of charge neutrality are assumed. Electron collision excitation of electronic molecular states, dissociation and ionization are not considered in the kinetic scheme since the electron temperature in the nitrogen post-discharge presents a low value (0.3 eV) as stated in the works of Gorbunov et al. [22, 23].

We observe that the PA ionization in the nitrogen flowing DC discharge is activated by reactions that depend on the $N_2(X\,^1\Sigma^+_g, v)$ states (see reactions (1) – (3)). Therefore there is a strong dependence on the $N_2(X\,^1\Sigma^+_g)$ vibrational distribution function (VDF) [24] in the post-discharge. The same dependence has been pointed out for the PA of the flowing nitrogen microwave discharge. However the ionization mechanisms acting in its post-discharge are quite different as will be shown. As discussed by the Lisbon team [11, 13, 14], the ionization in the PA of the microwave discharge is initiated with the excitation of molecular metastable states $N_2(A^3\Sigma^+_u)$ and $N_2(a'^1\Sigma^-_u)$:

$$N_2(X^1\Sigma^+_g), v > 38 + N(^4S) \rightarrow N(^2D) + N_2(A^3\Sigma^+_u) \text{ and} \qquad (10)$$

$$N_2(X^1\Sigma^+_g, v > 37) + N(^4S) \rightarrow N(^4S) + N_2(a'^1\Sigma^-_u). \qquad (11)$$

Then these metastables generate the ionization by Penning ionization reactions:

$$N_2(a'^1\Sigma^-_u) + N_2(a'^1\Sigma^-_u) \rightarrow N_2^+(X^2\Sigma^+_g) + N_2(X^1\Sigma^+_g) + e \text{ and} \qquad (12)$$

$$N_2(A^3\Sigma^+_u) + N_2(a'^1\Sigma^-_u) \rightarrow N_2^+(X^2\Sigma^+_g) + N_2(X^1\Sigma^+_g) + e. \qquad (13)$$

The $N_2^+(B^2\Sigma^+_u)$ ion excitation occurs via reaction (7) as in the PA of the DC discharge. We verify that PA ionization mechanisms of the DC and microwave discharges are initiated by excitation reactions depending on the $N_2(X\,^1\Sigma^+_g, v)$ states. In this sense

ionization strictly depends on the $N_2(X\,^1\Sigma_g^+)$ VDF evolution in the post-discharge. Still the Lisbon group has described this set of reactions as responsible for the ionization, they point out that $N(^2P)$ states can have an important role in the ionization of the PA. Popov [10] has shown that $N(^2P)$ states can explain the PA ionization in the nitrogen flowing microwave discharges by the atoms associative ionization mechanism:

$$N(^2P) + N(^2P) \rightarrow N_2^+(X^2\Sigma_g^+) + e. \qquad (14)$$
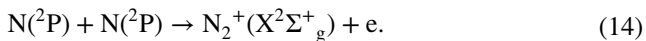
Another kinetic phenomena, as the molecular dissociation in the PA of the nitrogen flowing DC discharge, and $N_2(B^3\Pi_g)$ excitation mechanisms in the microwave discharges are discussed in previous works [6, 16, 25]. It is also observed that these mechanisms also strongly depend on the VDF in the post-discharge.

As it was shown in the literature [8, 26], the PA presents a gas temperature profile in the post-discharge. Gas temperature decreases from the end of the discharge down to the end of the post-discharge tube. The numerical kinetic models used to describe the PA global kinetics can assume two different approaches. In the first one, the post-discharge gas temperature is considered with a constant value representing a mean value of the post-discharge temperature profile, or a representative PA gas temperature. This value was assumed as 400 K in our previous work [15] and also in the work of Loureiro et al. [11]. In another works, we used the mean value of the measured gas temperature profile as a constant gas temperature representative value (T = 370 K) [9, 16, 17]. The second approach consists of measuring the spatial/temporal gas temperature profile in the post-discharge and to include it in the numerical kinetic model [8, 10, 13]. Both approaches produce reliable results in the PA modeling. However, until now, there is not a work analyzing the effects of these two different approaches in the global kinetics description of the PA phenomenon. Our present work provides a detailed analysis of the global kinetic features of the PA of the nitrogen flowing DC discharges assuming a mean constant value, and the measured gas temperature profiles in the modeling. We study the effects of such considerations in the density profiles of the $N_2^+(B^2\Sigma_u^+)$ excited ions, and also in some molecular singlet ($N_2(a'^1\Sigma_u^-)$), and triplet states ($N_2(A^3\Sigma_u^+)$, and $N_2(B^3\Pi_g)$). The $N_2^+(X^2\Sigma_g^+)$, N_3^+, and N_4^+ ions density profiles are also studied. We analyze the effects of such considerations in the pertinent reaction pathways concerning the studied species and $N_2(X\,^1\Sigma_g^+)$ VDFs.

2 Experimental Set-Up and Results

The experimental set-up utilized in the present work is presented in Fig. 1.

We studied the pure nitrogen discharges and post-discharges generated in the discharge and post-discharge tubes.

The tubes are made of Pyrex glass and have 1.4 cm inner diameter. The discharge zone consisting of the positive column occurs between the side armed electrodes, and initiates at the anode and ends at the cathode. The post-discharge initiates just at the end of the discharge zone downstream the flow of high purity nitrogen gas (99.999%) that is injected in the beginning of the discharge tube. Its flow rate is controlled by a flow meter (MKS 247C). The gas pressure is measured by a Baratron gauge (MKS 722A). The low pressure is maintained by a mechanical vacuum pump of 25 $m^3 h^{-1}$ (E1M18 Edwards). The emissions from the discharge and post-discharge regions are measured by a monochromator (Jobin-Yvon, THR-1000) with a grating of 1800 gr.mm^{-1} connected to a photomultiplier tube (Hamamatsu, R928). We use an optical fiber to collect the emitted light. The discharge electric field is maintained between the two side-armed electrodes located 20 cm apart in the discharge tube, by a high voltage direct current source. We use Double Langmuir probes located 10 cm apart inserted in the middle of the discharge tube for measurements of the voltage drop in the positive column. The discharge electric current was measured by an amperemeter connected to the discharge circuit. The reduced electric field (E/N) and electron density (n_e) (see the method to estimate the electron density in Ref. [27]) values of the positive column are obtained from the voltage drop, discharge current, and gas pressure. We estimate the $N_2(X^1\Sigma_g^+)$ vibrational temperature at the end of the discharge by Optical Emission Spectroscopy (OES), positioning the optical fiber transversely to the discharge tube near the cathode (see Fig. 1). We measure the emissions from the transitions of the second positive system in the range of 360 – 385 nm. We obtained the relative densities of the $N_2(C^3\Pi_u, v)$ states employing the following mathematical relation between emitted light intensity and the density of emitting species:

$$I_{v,w} = \frac{C(\lambda_{v,w})hc[N_v]A_{v,w}}{\lambda_{v,w}}, \qquad (15)$$

where $I_{v,w}$ is the light intensity, $C(\lambda_{v,w})$ is the optical system spectral response, $A_{v,w}$ are the transitions probabilities [20], $\lambda_{v,w}$ is the transition wavelength, h is the Planck constant, c is the light velocity and $[N_v]$ is the concentration of the emitting state. The $N_2(C^3\Pi_u, v)$ density distribution is linearized by discarding the overpopulated vibrational populations with respect to a Boltzmann distribution and the $N_2(X^1\Sigma_g^+, v)$ distribution is calculated on the basis of the Franck-Condon factors [28]. This procedure of the vibrational temperature estimation has been used in several works [7–9, 15–18, 25, 29]. The vibrational temperature is used in the post-discharge kinetic model as input for the initial $N_2(X^1\Sigma_g^+)$ VDF in the post-discharge. Near this range of wavelengths, we find the 391.4 nm band transitions from the first negative system
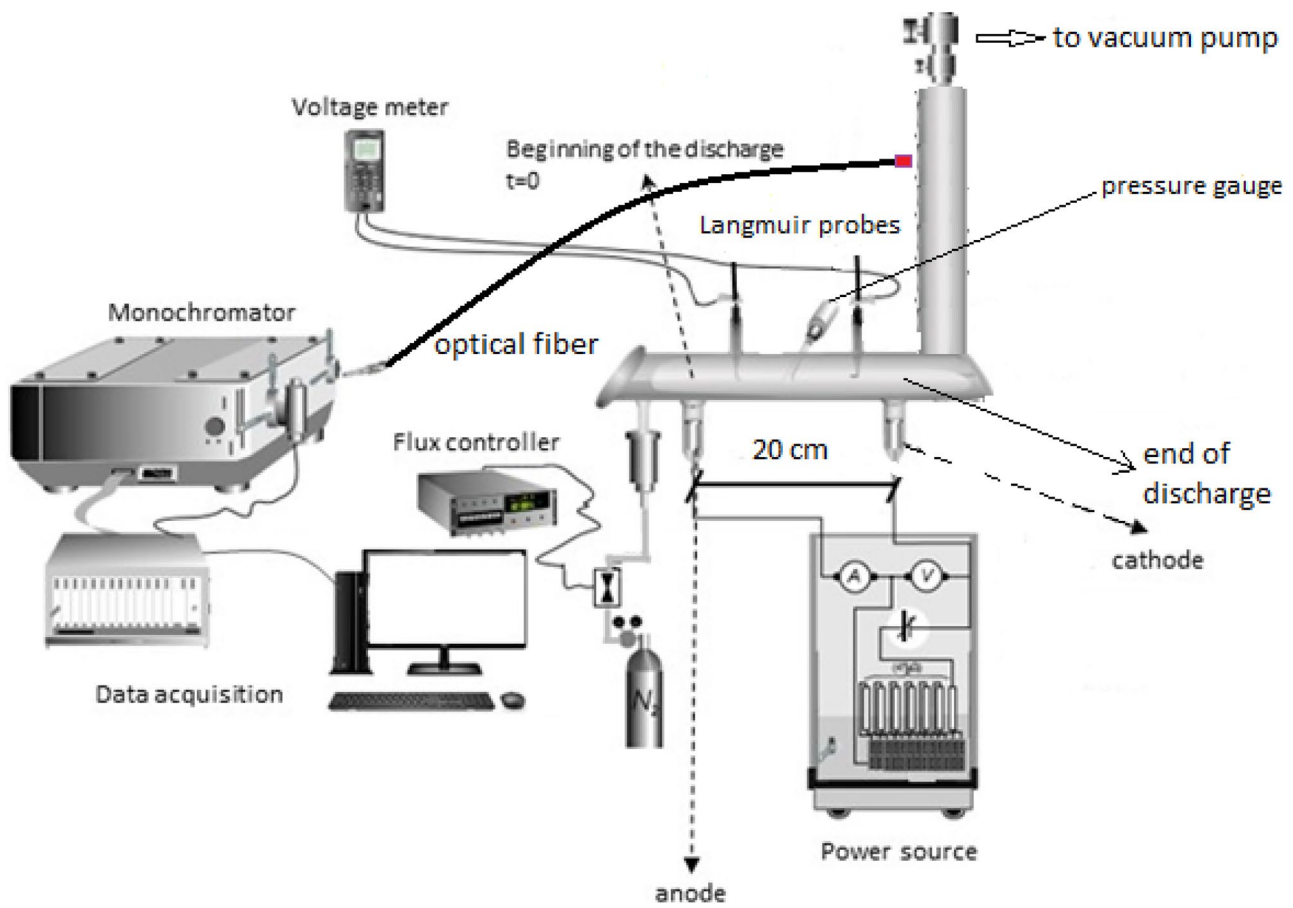
Fig. 1 Experimental set-up

originated from the $N_2^+(B^2\Sigma^+_u)$ ions. We use these band emissions and Eq. (15) to measure the relative density of such ions in the post-discharge. We present a typical spectrum relative to the mentioned transitions measured at the end of discharge in Fig. 2. The gas temperature was also measured by OES at the end of the positive column and along the post-discharge. We utilized the transitions of the first positive system of nitrogen molecules in the range of 760 – 780 nm [29, 30]. A typical spectrum of such transitions is shown in Fig. 3. The gas temperature is determined for our optical system from the ratio of P1(774.8 nm) and P2(773.5 nm) intensities following the work of Hochard et al.[30]. The gas temperature in K follows the equation:

$$T(P1, P2) = 183.3 + 506\exp((0.8 - P1/P2)/0.23)). \quad (16)$$

In this work, we analyze two different experimental conditions where the PA occurs in the post-discharge tube. They are: **(1)** p = 250 Pa (gas pressure), I = 45 mA (discharge current), and Q = 0.6 Sl m^{-1} (gas flow rate); **(2)** p = 500 Pa, I = 30 mA, and Q = 0.5 Sl m^{-1}. The discharge experimental parameters for these experimental conditions are expressed in Table 1. The voltage drop measured in the

Langmuir probes placed in the middle of the discharge´s electrodes are: V = 196 ± 5 V for discharge condition (1) and V = 187 ± 4 V for discharge condition (2). These data will be utilized as input parameters in the kinetic numerical models for the positive column and post-discharge. The n_e, E/N, and n_e/N parameters are used in the positive column kinetic model in the calculation of the electron energy distribution function (EEDF) of the discharge [27]. The vibrational temperature (T_v) measured at the end of the positive column is used as characteristic temperature of a Boltzmann distribution considered as the initial $N_2(X^1\Sigma^+_g)$ VDF in the post-discharge modeling [8, 9, 15]. The discharge gas residence time τ is used to determine the time corresponding to the end of the discharge. Initial densities of species considered in the post-discharge model are obtained from the positive column kinetic model at the end of the discharge residence time.

As a key result in our study, we determined the gas temperature profile in the post-discharge, with measurements initiating at the end of the discharge (see Fig. 1) and extending along the post-discharge tube (see Fig. 1). The temperature profiles found as functions of the spatial coordinate were

Fig. 2 Emission spectrum from 360 – 395 nm wavelengths recorded at the end of the discharge zone (see Fig. 1). The emissions are originated from the second positive and first negative systems of nitrogen molecules [20]
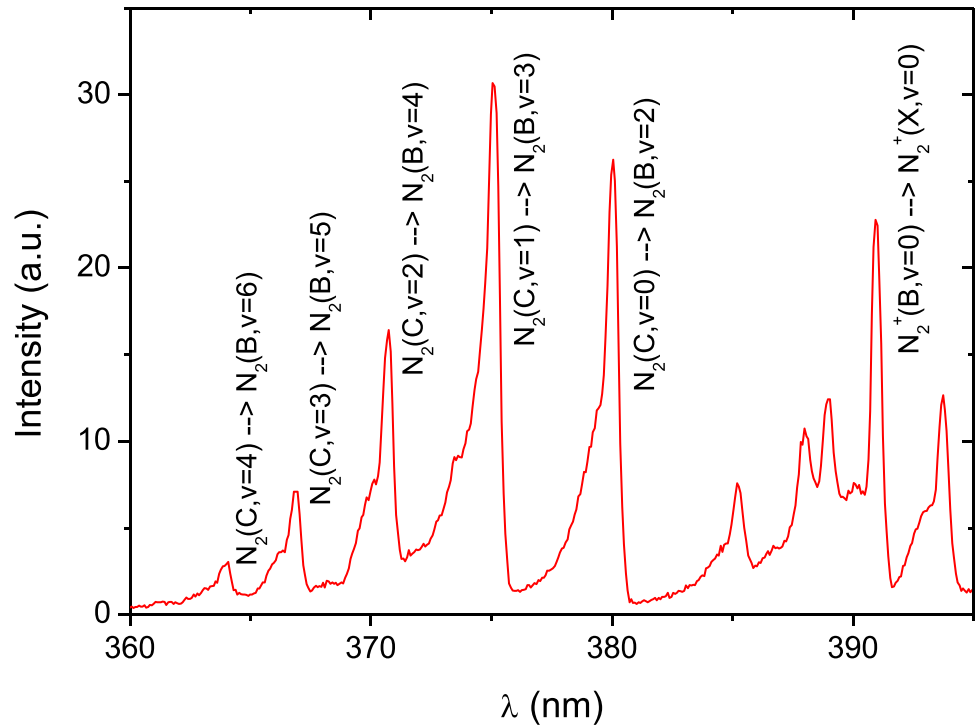
converted to gas temperature profiles as functions of the post-discharge gas residence time. We use the mathematical relation between the post-discharge position (x) and the gas velocity (v) for the conversion of the spatial coordinate to post-discharge gas residence time. The detailed description of such procedure is presented in Ref. [16]. The temperature measurements for the studied discharge conditions ((1) and (2)) are presented in Fig. 4. The temperature errors were calculated from the error estimated in Ref. [30] merged to the P1 and P2 fluctuations for several measurements at the same experimental condition and propagated following Eq. (16).

Fig. 3 Emission spectrum from 760 – 780 nm wavelengths recorded at the end of the discharge zone (see Fig. 1). The emissions are originated from the transitions of the first positive system of nitrogen molecules [20, 29, 30]
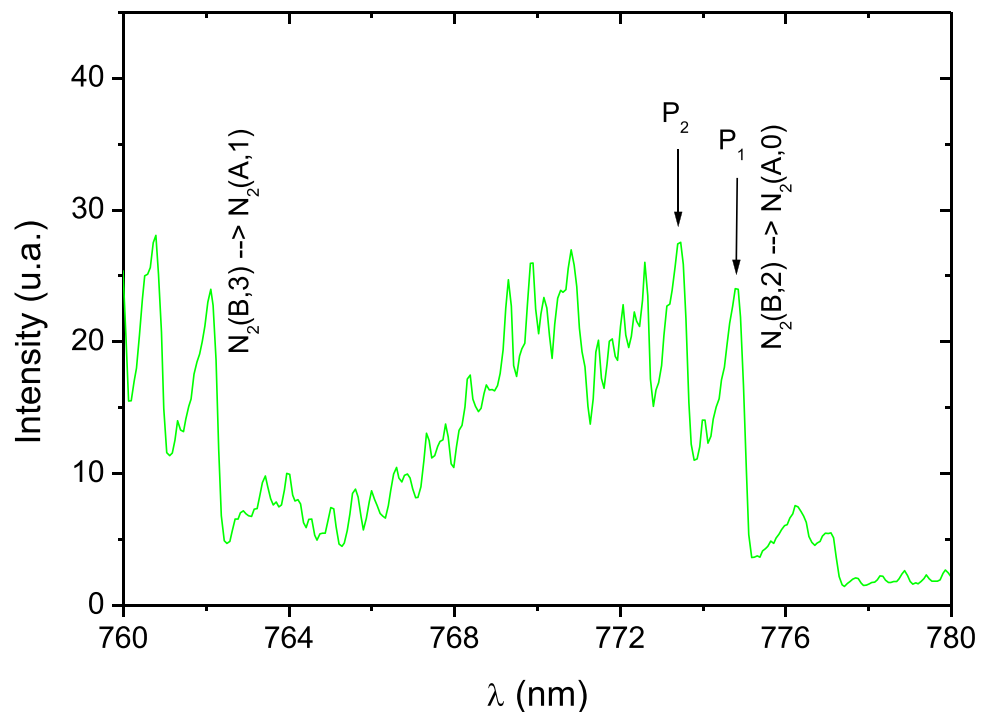
Table 1 Experimental discharge parameters: electron density (n_e), $N_2(X^1\Sigma^+_g)$ vibrational temperature (T_v), gas residence time (τ), reduced electric field (E/N), and degree of ionization (n_e/N)

Discharge condition	n_e ($\times 10^9$ cm^{-3})	T_v ($\times 10^2$ K)	τ (ms)	E/N (Td)	n_e/N
(1)	42.0 ± 1.0	64 ± 9	4.8 ± 1.0	47 ± 5	10^{-6}
(2)	57.0 ± 2.0	51 ± 8	8.6 ± 1.5	30 ± 3	9×10^{-7}

We have fitted the mathematical functions for the gas temperature variation. These functions are:

$$T1(t) = 297.26 + 135\exp(-t/0.00667) \quad \text{(discharge condition(1))} \quad \text{and} \tag{17}$$

$$T2(t) = 328.4 + 254.61\exp(-t/0.0062) \quad \text{(discharge condition(2))}, \tag{18}$$

where t is the post-discharge residence time in seconds. We will employ these functions in the calculations of the species densities with the post-discharge kinetic model in the next section.

3 Results and Discussion

The aim of this work is to carry out an analysis of the pink afterglow kinetic modeling under two different assumptions. In the first one, we consider the post-discharge gas temperature with a constant representative value [11, 15]. In the second assumption, the measured post-discharge gas temperature profile is utilized in the numerical code to account for effects of gas temperature variation in the several kinetic mechanisms that depend on this parameter. To accomplish this task we employed a well-established kinetic numerical model for the nitrogen post-discharge [7–9, 15–18]. This is a 0-D kinetic model that integrates in time the coupled rate balance equations for the considered species together with the master vibrational equation (VME) for the $N_2(X^1\Sigma^+_g, v)$ states, which includes the V-V and V-T exchange reactions [15]. The considered species are: $N_2(X^1\Sigma^+_g, 0 \le v \le 45)$, $N_2(A^3\Sigma^+_u)$, $N_2(B^3\Pi_g)$, $N_2(a^1\Pi_g)$, $N_2(a'^1\Sigma^-_u)$, $N_2(a''^1\Sigma^+_g)$, $N_2(C^3\Pi_u)$, $N_2^+(X^2\Sigma^+_g)$, $N_2^+(B^2\Sigma^+_u)$, N^+, N_3^+, N_4^+, $N(^4S)$, $N(^2D)$, and $N(^2P)$. We consider 66 physical-chemical processes between the neutral and excited molecules, atoms, and ions [8]. The kinetic model furnishes the species densities as a function of the post-discharge residence time. This model requires as entries the initial $N_2(X^1\Sigma^+_g)$ VDF (t = 0) and the densities of species at the end of the positive column, or the beginning of the post-discharge. We consider the initial VDF as a Boltzmann function with the measured vibrational temperature acquired at the end of the discharge [8, 9, 15, 18, 25] (see the T_v values in Table 1). The initial $N_2^+(X^2\Sigma^+_g)$ density is assumed equal to the measured electron density (see the n_e values in Table 1) and the other ions initial densities are assumed equal zero [7–9, 15–18, 25]. The ions initial density distribution rapidly (0.01 ms) reaches a new equilibrium distribution due the ion transfer reactions considered in the kinetic model [15, 18]. The atomic and molecular states
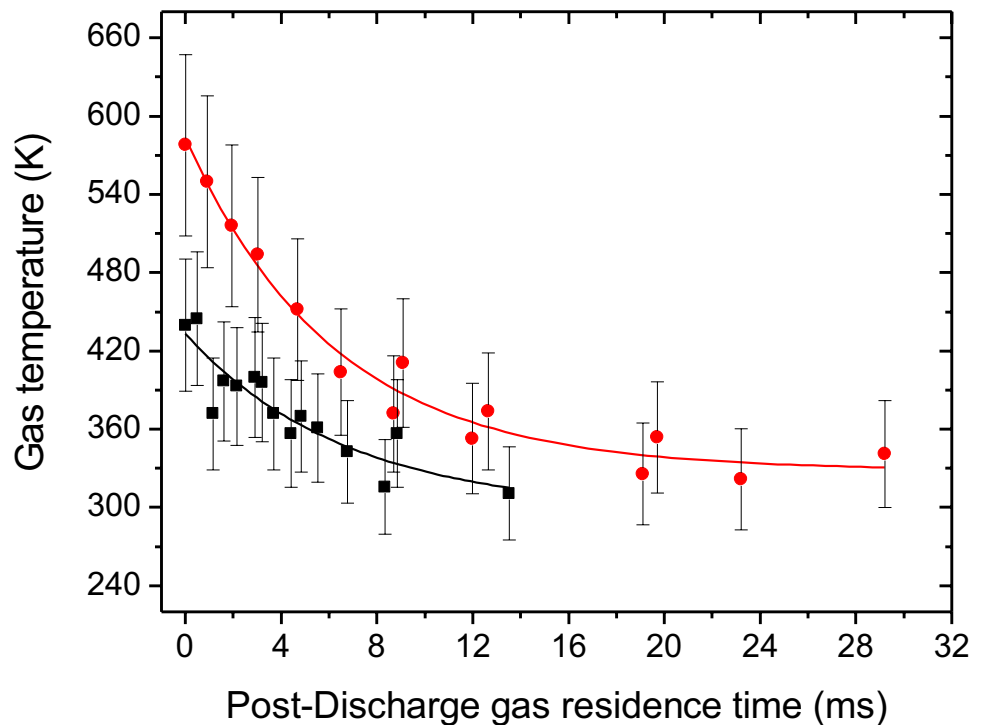

Fig. 4 Post-discharge gas temperature as function of the post-discharge gas residence time. The square symbols refer to discharge condition (1). The circle symbols refer to discharge condition (2)

Fig. 5 $N_2^+(B^2\Sigma^+_u)$ experimental and calculated densities for discharge condition (1) (see Table 1). The red line is the calculated density for a constant post-discharge gas temperature ($T = 370$ K). The green line is the calculated density for the post-discharge gas temperature following Eq. (17). The square symbols represent the experimental ion density measured by OES (see experimental section)
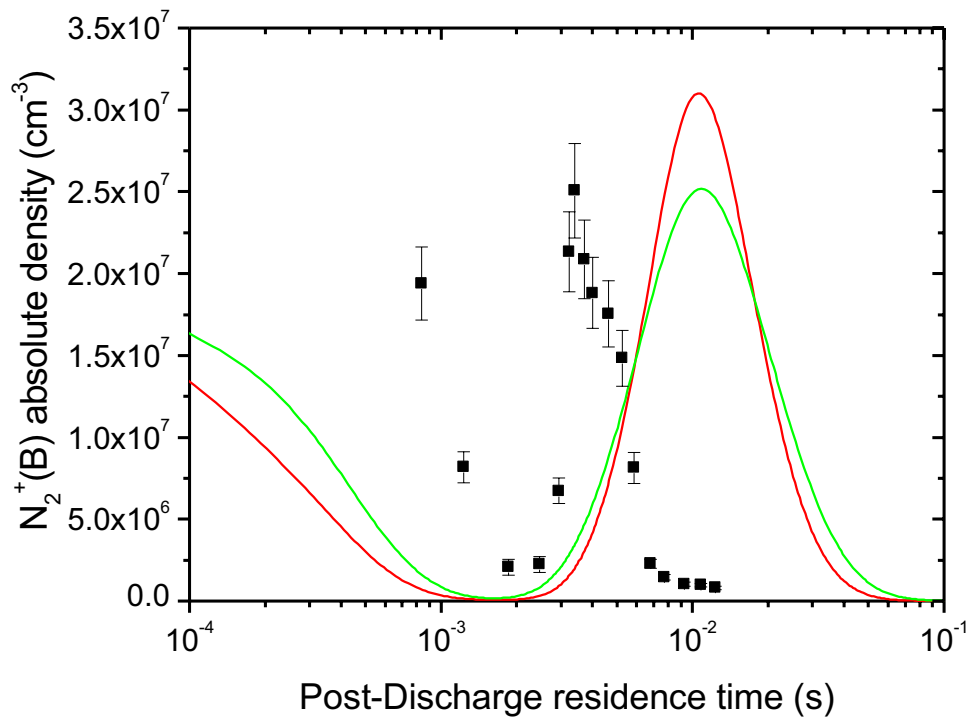
initial densities considered in the post-discharge model are taken from another kinetic numerical model developed to describe the positive column [27]. This discharge model has been recently used to describe the kinetics of ionization [18] and dissociation [25] phenomena in the flowing nitrogen DC discharges. The discharge kinetic model furnishes the species densities as a function of the discharge residence time. We consider the calculated densities at the end of the discharge as the post-discharge initial densities (see the discharge gas residence times in Table 1).

Here, the post-discharge kinetic model assumes two different approaches. In the first, we calculate the species densities for a fixed post-discharge gas temperature value. We determined the post-discharge mean gas temperature values from our measurements (see Figure 4) and found $<T> = 370$ K for the discharge condition (1) and $<T> = 420$ K for the discharge condition (2). In the second, we employ the post-discharge gas temperature variation, from Eqs. (17) and (18), to calculate the species densities for our experimental conditions (see Table 1).

We begin our analysis with the calculation of the $N_2^+(B^2\Sigma^+_u)$ density as a function of the post-discharge residence time. We calculated the density for the experimental condition (1), for a fixed gas temperature of 370 K, and for the measured post-discharge gas temperature profile (see eq.(17)). The calculated densities were compared to the experimental $N_2^+(B^2\Sigma^+_u)$ density obtained from the transitions of the first negative system at 391.4 nm wavelength (see Figure 2). These results are shown in Figure 5. The experimental relative ion density was normalized to the

$N_2^+(B^2\Sigma^+_u)$ calculated density at the maximum of the PA ($t \sim 10$ ms) (see the green curve in Figure 5). We can observe that the $N_2^+(B^2\Sigma^+_u)$ calculated densities present their maxima at $t \sim 10$ ms. The calculated density at the PA maximum is a little higher when the post-discharge gas temperature is considered with a constant value. The experimental density has its maximum value at $t \sim 3.5$ ms. The minimum values of the calculated densities and the experimental one occur at $t \sim 2$ ms. The increasing behavior of the curves, before the maximum is attained, is more pronounced in the experimental density than in the calculated ones. In a general way there is a reasonable agreement in the behavior of the experimental and calculated densities. This shift in time between the calculated and experimental densities behavior has been observed in a previous study [17].

Once we have studied the post-discharge excited ion density profiles we will analyze the $N_2(A^3\Sigma^+_u)$ and $N_2(a'^1\Sigma^-_u)$ metastable states. The metastables calculated densities for discharge conditions (1) and (2) are presented in Figures 6 and 7, respectively. We have calculated the densities for a constant mean gas temperature ($T = 370$ K for discharge condition (1) and $T = 420$ K for discharge condition (2)), and for the measured gas temperature profiles (equations (17) and (18)).

In a general way, the calculated densities for the constant gas temperature and for the measured gas temperature profiles present a very similar behavior. As it has happened to the excited ions (see Figure 5), the calculated densities for the constant gas temperature are higher than the densities obtained for the measured gas temperature profiles

Fig. 6 Post-discharge
$N_2(A^3\Sigma_u^+)$ (black lines) and
$N_2(a'^1\Sigma._u^-)$ (red lines) calcu-
lated densities for discharge
condition (1). The dashed lines
are the densities for a post-dis-
charge constant gas temperature
(370 K). The solid lines are the
densities for the post-discharge
gas temperature following
Eq. (17) (see experimental
section)
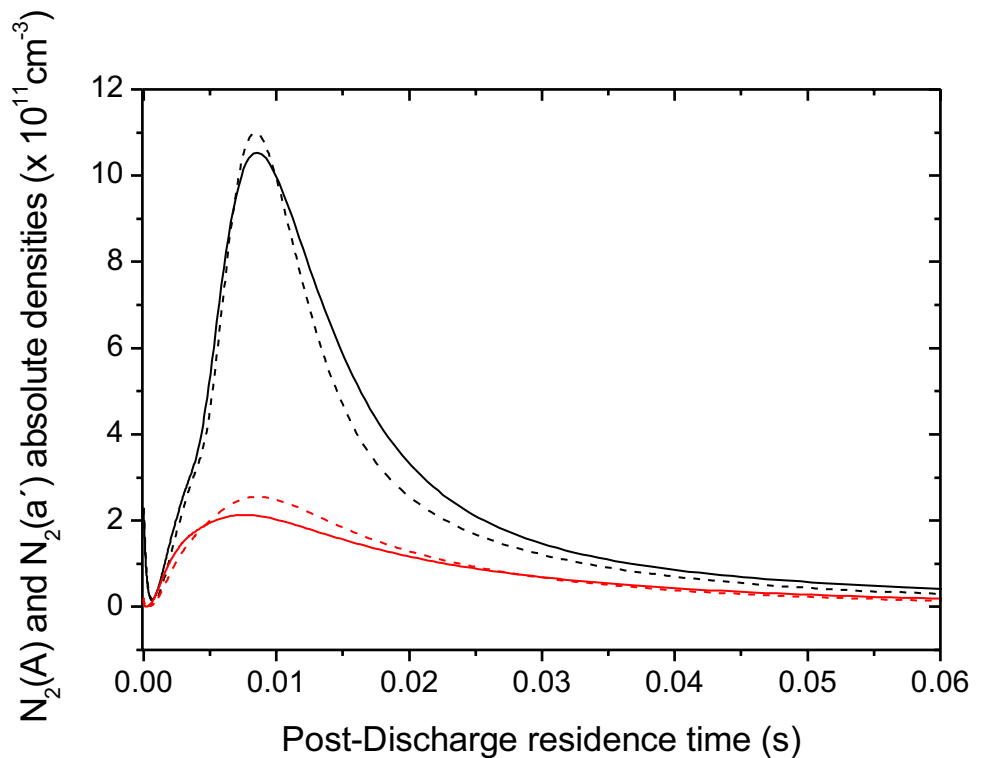
at the PA maximum. We also observe that the maximum
densities for the measured gas temperature profiles occur at
shorter gas residence times when compared to the calculated
densities for the constant gas temperature. The metastable

densities minimum values occur at residence times between
0.2 to 0.7 ms and the maximum values occur at residence
times between 5.5 and 8.5 ms. Also, the decreasing behavior
of the densities after the maximum density is reached are

Fig. 7 Post-discharge
$N_2(A^3\Sigma_u^+)$ (black lines) and
$N_2(a'^1\Sigma._u^-)$ (red lines) calcu-
lated densities for discharge
condition (2). The dashed lines
are the densities for a post-dis-
charge constant gas temperature
(420 K). The solid lines are the
densities for the post-discharge
gas temperature following
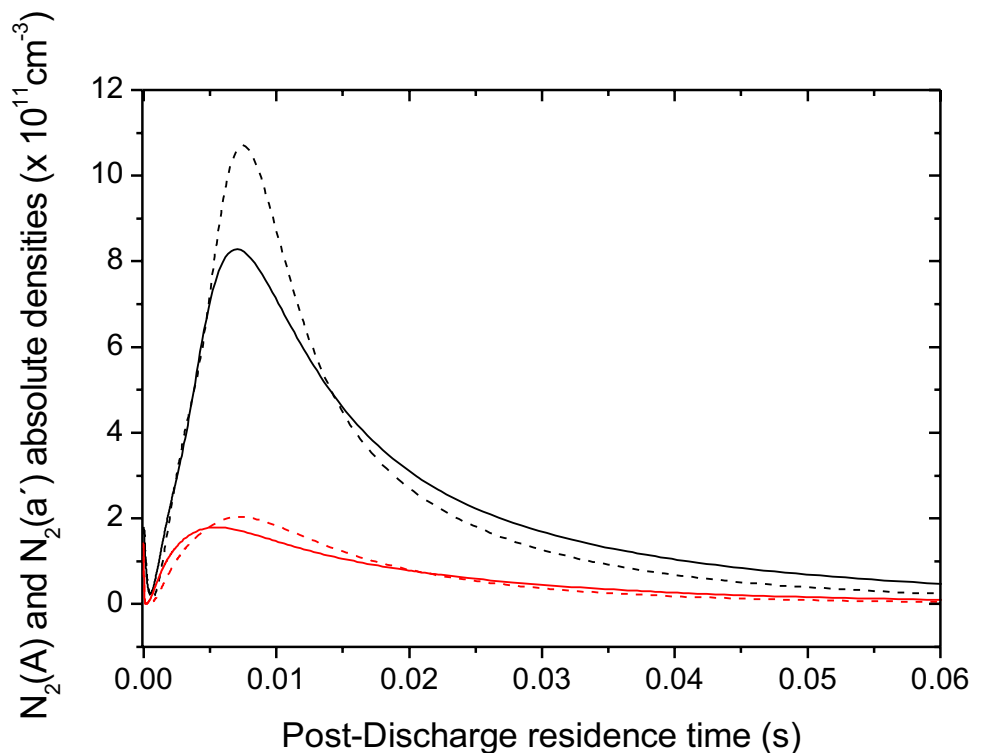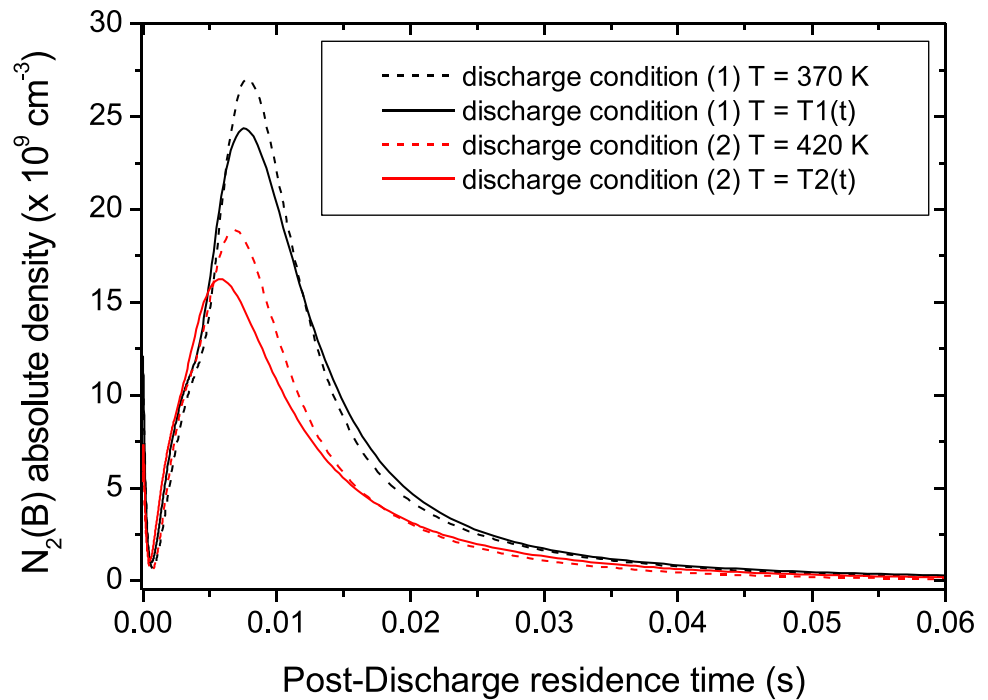Eq. (18) (see experimental
section)

Fig. 8 Post-discharge $N_2(B^3\Pi_g)$ calculated density for discharge condition (1) (black lines) and condition (2) (red lines). The solid lines represent the calculations for the measured gas temperature profiles (see Eqs. (17) and (18)) and the dashed lines the calculations for the constant gas temperature assumption

more pronounced in the case of the constant gas temperature assumption. We will deepen the analysis after the presentation of the remaining results concerning the other species behavior.

The calculated density profiles of the triplet state $N_2(B^3\Pi_g)$ for both experimental discharge conditions are presented in Figure 8.

We can firstly observe that minimum densities for the $N_2(B^3\Pi_g)$ state present similar values for both the discharge conditions. However, the maximum calculated densities are stronger for discharge condition (1). In this sense the PA is more excited for this discharge condition. The same occurs with the $N_2(A^3\Sigma_u^+)$ and $N_2(a'^1\Sigma_u^-)$ calculated densities. This fact can be understood as a direct result of the

Fig. 9 Post-discharge ions calculated densities as functions of the post-discharge residence time. The curves are specified in the figure legend
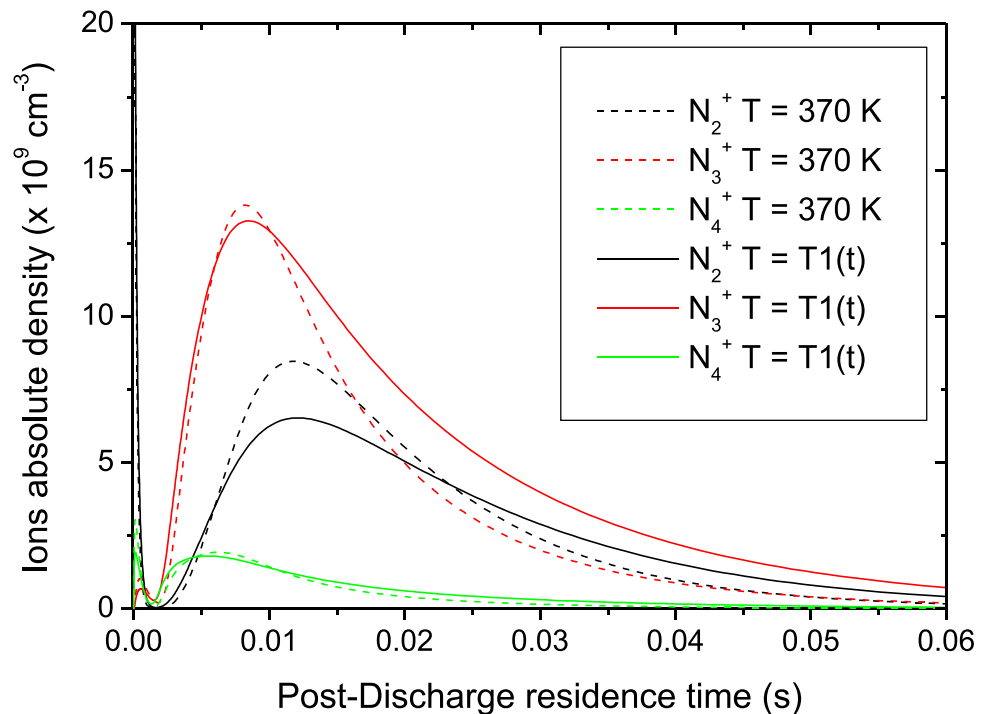
Table 2 Residence times corresponding to the maximum densities in the PA and their values (discharge condition (1))

Species discharge condition (1)	t1 (370 K) (ms)	t2 T1(t) (ms)	$\rho1$ (370 K) (cm^{-3})	$\rho2$ T1(t) (cm^{-3})	t1/t2	$\rho1/\rho2$
$N_2(A)$	8.5	8.5	1.1×10^{12}	1.05×10^{12}	1	1.05
$N_2(a')$	8.3	7.5	2.6×10^{11}	2.1×10^{11}	1.11	1.24
$N_2(B)$	7.8	7.6	2.7×10^{10}	2.4×10^{10}	1.03	1.12
$N_2^+(X)$	11.9	12.1	8.4×10^{9}	6.6×10^{9}	0.98	1.27
N_3^+	8.3	8.7	1.4×10^{10}	1.3×10^{10}	0.95	1.08
N_4^+	6.1	5.5	2×10^{9}	1.8×10^{9}	1.11	1.11

Time for the constant gas temperature approximation (t1). Time for the measured gas temperature T1(t) (see Eq. (17)) (t2). Maximum calculated densities for the constant gas temperature approximation ($\rho1$) and for the measured gas temperature ($\rho2$)

higher vibrational excitation of discharge condition (1) at the beginning of the post-discharge (see measured discharge vibrational temperatures in Table 1). As we have observed for the $N_2(A^3\Sigma^+_u)$ and $N_2(a'^1\Sigma^-_u)$ calculated densities, the $N_2(B^3\Pi_g)$ calculated density profiles for a constant gas temperature and for the measured gas temperature profiles have a similar behavior in the post-discharge. Again, the calculated densities at the PA maximum are a few higher for the constant gas temperature assumption. Also, the $N_2(B^3\Pi_g)$ maximum densities occur later in the post-discharge for the constant gas temperature approximation. The density decreasing behavior after the maximum density is attained is more pronounced for the constant gas temperature cases. Finally, we present in Figure 9 the calculated ions density profiles in the post-discharge. We find that the ions density distribution follows the experimentally observed behavior in the PA, that is, the N_3^+ ion is the dominant ionic species followed by the $N_2^+(X^2\Sigma^+_g)$, and N_4^+ ions [1]. As follows with the singlet and triplet molecular states, the ions densities are higher at the PA maximum for the constant gas temperature approximation. The ions density maxima occur in the time interval between 5 and 12 ms. Differently from the studied molecular states, the $N_2^+(X^2\Sigma^+_g)$ and N_3^+ maximum densities occur at shorter residence times when the constant gas temperature approximation is assumed. In order to get a better understanding on the studied species behavior under the two different approaches, the post-discharge constant gas temperature and the measured gas temperature profiles approximations, we developed Tables 2 and 3 that

contain the residence times of species maximum densities and their values. We also calculated the ratio between the residence times and for the densities for the two gas temperature approximations.

From Table 2 and 3, it can be more detailed seen the behavior of studied species presented in Figs. 6, 7, 8 and 9. The singlet and triplet molecular states residence times corresponding to the maximum densities in the PA occur between 5.5 and 8.5 ms, being those ones referring to the constant gas temperature approximation longer than the residence times corresponding to the measured gas temperature profiles approximation. We see from the residence time ratios (5th column in Table 2 and 3) that the difference in both approaches results in longer residence times for the constant gas temperature approximation with maximum difference value of 33% for the $N_2(a'^1\Sigma^-_u)$ state in the discharge condition (2) (see Table 3). The density values at the PA maximum are from 5 to 32% higher in the constant gas temperature approximation (see 6th column of Table 2 and 3), being the highest one that for the $N_2(A^3\Sigma^+_u)$ state at discharge condition (2). At this point, after verifying the density profiles behavior of the analyzed species, we can argue in favor of the post-discharge constant gas temperature approximation as a reliable method to be employed in the kinetic numerical modeling of the PA. The differences in the density profiles are not too expressive and, in the absence of the measured post-discharge gas temperature profiles, the constant gas temperature approximation seems a useful tool in the post-discharge kinetic modeling. We will now analyze

Table 3 Residence times corresponding to the maximum densities in the PA and their values (discharge condition (2))

Species discharge condition (2)	t1 (420 K) (ms)	t2 T2(t) (ms)	$\rho1$ (420 K) (cm^{-3})	$\rho2$ T2(t) (cm^{-3})	t1/t2	$\rho1/\rho2$
$N_2(A)$	7.4	7.1	1.1×10^{12}	8.3×10^{11}	1.04	1.32
$N_2(a')$	7.3	5.5	2.0×10^{11}	1.8×10^{11}	1.33	1.11
$N_2(B)$	6.8	5.7	1.9×10^{10}	1.6×10^{10}	1.19	1.19

Time for the constant gas temperature approximation (t1). Time for the measured gas temperature T2(t) (see Eq. (18)) (t2). Maximum calculated densities for the constant gas temperature approximation ($\rho1$) and for the measured gas temperature ($\rho2$)

Table 4 $N_2(A^3\Sigma^+_u)$ excitation processes

Process:	Two-body reaction	k (cm^{3}s^{-1})	Ref.
	Spontaneous emission	ν (s^{-1})	
A1	$N_2(B^3\Pi_g) + N_2(X\ ^1\Sigma_g^+) \rightarrow N_2(A^3\Sigma^+_u) + N_2(X\ ^1\Sigma_g^+)$	2.85×10^{-11}	[31]
A2	$N_2(B^3\Pi_g) \rightarrow N_2(A^3\Sigma^+_u) + h\nu$	2.4×10^5	[20]
A3	$N_2(X\ ^1\Sigma_g^+, v > 24) + N(^4S) \rightarrow N_2(A^3\Sigma^+_u) + N(^4S)$	10^{-15}	[11, 32]
A4	$N_2(X\ ^1\Sigma_g^+, v = 10) + N(^2P) \rightarrow N_2(A^3\Sigma^+_u) + N(^4S)$	8.6×10^{-11} x $\frac{1 - e^{\frac{2062}{T}}}{1 - e^{\frac{3353}{T}}} e^{\frac{-1398}{T}}$	[33]
A5	$2 \times N_2(X\ ^1\Sigma_g^+, v > 11) \rightarrow N_2(A^3\Sigma^+_u) + N_2(X\ ^1\Sigma_g^+, v = 0)$	10^{-17}	[11, 32]

the kinetic aspects that bring such differences in the post-discharge density profiles for the two different approaches concerning the post-discharge gas temperature. An important aspect concerning the kinetics of the studied species is their excitation rates. The excited states excitation rates determine the behavior of the density profiles in the post-discharge. Here, we will focus in the $N_2(A^3\Sigma^+_u)$, $N_2(B^3\Pi_g)$, and $N_2(a'^1\Sigma^-_u)$ states. Our kinetic numerical model accounts for 66 physical–chemical processes between the considered species [8]. The kinetic processes concerning the $N_2(A^3\Sigma^+_u)$ generation are presented in Table 4. The excitation rates of each process are defined as the product of the reactants concentration and the rate constant of each reaction.

The $N_2(A^3\Sigma^+_u)$ excitation rates of reactions A1 – A5, for the discharge condition (2), are shown in Fig. 10. It should be noted that this discharge condition produces the highest difference in the $N_2(A^3\Sigma^+_u)$ calculated densities at the PA maximum, as can be verified by inspection of Table 2 and 3. We have calculated the excitation rates for the constant gas temperature approximation (T = 420 K) and for the

measured gas temperature profile (see Eq. (18)). It can be seen that the two different approaches for the gas temperature affect all the excitation mechanisms even though that only reaction A4 has a direct dependence on the gas temperature parameter expressed in its rate constant. It is verified that the dominant $N_2(A^3\Sigma^+_u)$ excitation channel is the $N_2(B^3\Pi_g)$ quenching by the nitrogen molecules (reaction A1). Focusing on this excitation mechanism, we verify that the excitation rates for the constant gas temperature approximation have their maximum value at longer post-discharge residence time and with a higher absolute value as compared to the excitation rates for the measured gas temperature approximation. This fact explains why the $N_2(A^3\Sigma^+_u)$ density profile for the constant gas temperature approximation presents a higher value occurring at longer post-discharge residence time as compared to the density profile for the measured gas temperature approximation (see black lines in Fig. 7). Moreover, if we compare the excitation rates of reaction A1 after their maximum values are attained, we verify that the rates are higher for the

Fig. 10 $N_2(A^3\Sigma^+_u)$ excitation rates for the constant gas temperature approximation (dashed lines) and for the measured gas temperature profile (solid lines). The reactions are: A1 (black lines), A2 (red lines), A3 (green lines), A4 (blue lines), and A5 (cyan lines) (see Table 4)
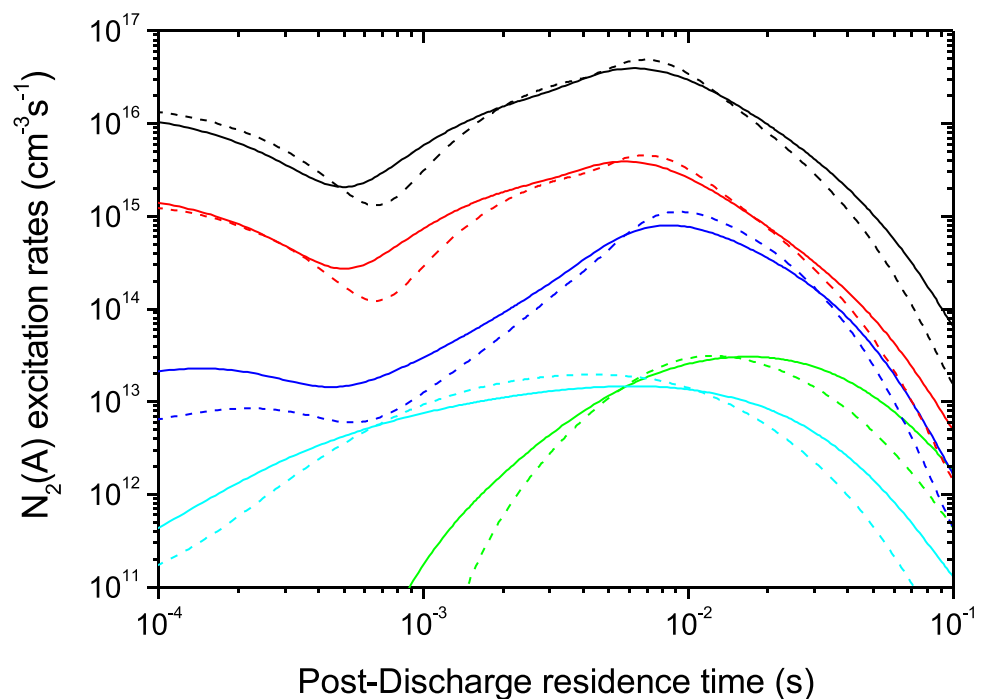
Table 5 $N_2(B^3\Pi_g)$ excitation processes

Process:	Two-body reaction	k (cm^{3}s^{-1})	Ref.
	Spontaneous emission	ν (s^{-1})	
	Three-body reaction	k (cm^{6}s^{-1})	
B1	$N_2(A^3\Sigma^+_u) + N_2(A^3\Sigma^+_u) \rightarrow N_2(B^3\Pi_g) + N_2(X\ ^1\Sigma^+_g, v=0)$	7.7×10^{-11}	[34]
B2	$N_2(C^3\Pi_u) \rightarrow N_2(B^3\Pi_g) + h\nu$	2.74×10^7	[20]
B3	$N_2(a'^1\Sigma^-_u) + N_2(X\ ^1\Sigma^+_g) \rightarrow N_2(B^3\Pi_g) + N_2(X\ ^1\Sigma^+_g)$	1.9×10^{-13}	[35]
B4	$N_2(A^3\Sigma^+_u) + N_2(X\ ^1\Sigma^+_g, 4<v<15) \rightarrow N_2(B^3\Pi_g) + N_2(X\ ^1\Sigma^+_g, v=0)$	2×10^{-11}	[31]
B5	$N(^4S) + N(^4S) + N_2(X\ ^1\Sigma^+_g) \rightarrow N_2(B^3\Pi_g) + N_2(X\ ^1\Sigma^+_g)$	2.4×10^{-33}	[36]

measured gas temperature approximation. This behavior explains the slower decrease of the $N_2(A^3\Sigma^+_u)$ density profile after its maximum value is reached in the density profile obtained for the measured gas temperature approximation (see the solid black line in Fig. 7). We will now analyze the $N_2(B^3\Pi_g)$ excitation rates for the two gas temperature assumptions in the post-discharge. The $N_2(B^3\Pi_g)$ excitation mechanisms considered in our kinetic numerical model are shown in Table 5.

The excitation rates of reactions B1 – B5, for the discharge condition (2), are shown in Fig. 11. At this discharge condition, it occurs the highest difference in the $N_2(B^3\Pi_g)$ calculated densities at the PA maximum, as can be verified by inspection of Table 2 and 3. As a first observation, the reaction B4 is the main $N_2(B^3\Pi_g)$ excitation mechanism in the post-discharge. This reaction has been evidenced as the main production mechanism for this triplet state also in the PA of the microwave flowing discharge [6]. As it has

been verified for the $N_2(A^3\Sigma^+_u)$ excitation mechanisms (see Fig. 10), all the $N_2(B^3\Pi_g)$ excitation pathways are affected by the different assumptions on the gas temperature in the post-discharge, even though these mechanisms present rate constants that do not depend directly on the gas temperature parameter (see Table 5). This fact indicates that the post-discharge global kinetics is affected by the different approaches on the gas temperature. We will return to this topic after the complete analysis of the studied species excitation rates. It can also be observed in the rates of reaction B4 that those ones concerning the constant gas temperature approximation present a higher maximum value occurring at a longer residence time with respect to the those ones in the measured gas temperature approach. This fact corroborates to the observed $N_2(B^3\Pi_g)$ density profiles behavior, that is, the maximum density of this state occurring later and with a higher absolute value when the constant gas temperature assumption is done. Also, the excitation

Fig. 11 $N_2(B^3\Pi_g)$ excitation rates for the constant gas temperature approximation (dashed lines) and for the measured gas temperature profile (solid lines). The reactions are: B1 (black lines), B2 (red lines), B3 (green lines), B4 (blue lines), and B5 (cyan lines) (see Table 5)
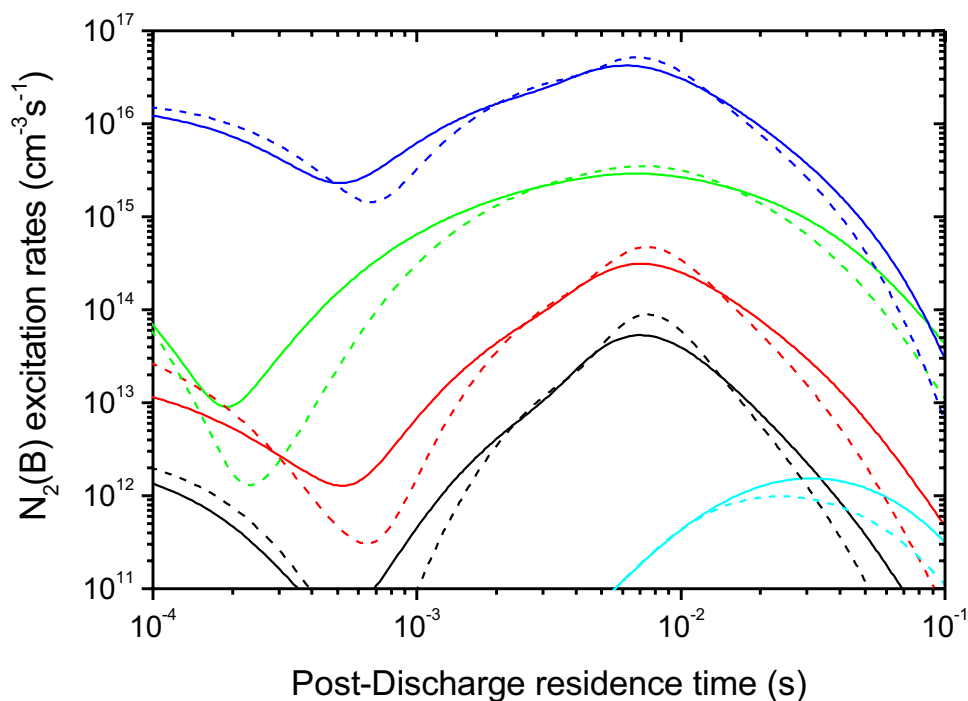
Table 6 $N_2(a'^1\Sigma^-_u)$ excitation processes

Process:	Two-body reaction Spontaneous emission	k (cm^{3}s^{-1}) ν (s^{-1})	Ref.
C1	$N_2(C^3\Pi_u) + N_2(X\ ^1\Sigma_g^+) \rightarrow N_2(a'^1\Sigma^-_u) + N_2(X\ ^1\Sigma_g^+)$	10^{-11}	[36]
C2	$N_2(a^1\Pi_g) + N_2(X\ ^1\Sigma_g^+) \rightarrow N_2(a'^1\Sigma^-_u) + N_2(X\ ^1\Sigma_g^+)$	9.1×10^{-12}	[37]
C3	$N_2(a^1\Pi_g) \rightarrow N_2(a'^1\Sigma^-_u) + h\nu$	1.91×10^2	[38]
C4	$N_2(X\ ^1\Sigma_g^+, v>37) + N(^4S) \rightarrow N_2(a'^1\Sigma^-_u) + N(^4S)$	10^{-12}	[39]
C5	$2\times N_2(X\ ^1\Sigma_g^+, v>15) \rightarrow N_2(a'^1\Sigma^-_u) + N_2(X\ ^1\Sigma_g^+, v=0)$	$2.1\times10^{-14}e^{\frac{-700}{T}}$	[36]

rates for the measured gas temperature approach present higher values after the maximum value is reached, causing a slower density decrease after the maximum in this case (see solid lines in Fig. 8).

Finally, we will analyze the $N_2(a'^1\Sigma^-_u)$ excitation rates for the discharge condition (1), where the difference in the maximum densities obtained for the constant gas temperature and the measured gas temperature approaches present the highest value (see Table 2 and 3). The excitation kinetic mechanisms for the singlet state are shown in Table 6. The excitation rates are shown in Fig. 12. Again, as observed for the other molecular states, the difference in the gas temperature assumptions affects all the excitation kinetic mechanisms. We should note that only reaction C5 has the gas temperature dependence in its rate constant. From Fig. 12, it is observed that reactions C2 and C5 are the dominant $N_2(a'^1\Sigma^-_u)$ excitation mechanisms. We should note that the $N_2(a^1\Pi_g)$ state, which is a reactant in reaction C2, also is generated by $N_2(X\ ^1\Sigma_g^+, v)$ states in a reaction similar to reaction (3) [8, 27]. Also, we observe that excitation rates

from reactions C2 and C5 present higher maximum values occurring at longer residence times for the constant gas temperature approximation as compared to the measured gas temperature approach. This fact explains the behavior of the $N_2(a'^1\Sigma^-_u)$ densities for the constant gas temperature assumption, which have their maximum densities higher than those ones found for the measured gas temperature assumption and occurring at longer residence times (see the red lines in Figs. 6 and 7). At this point, after the analysis of the molecular states excitation rates and density profiles, we conclude that a global kinetic effect is occurring in the PA modeling for the different post-discharge gas temperature assumptions. As it will be shown, this global effect occurs due the gas temperature approaches influence in the post-discharge VDFs. As well discussed in the literature [6, 15, 25], the atomic, molecular, and ionic states are generated directly or indirectly by the $N_2(X\ ^1\Sigma_g^+, v)$ states that depend on the VDFs behavior in the post-discharge. We should note that VDFs behavior depends on the vibrational-vibrational (V-V) and vibrational-translational (V-T) exchange reactions

Fig. 12 $N_2(a'^1\Sigma^-_u)$ excitation rates for the constant gas temperature approximation (dashed lines) and for the measured gas temperature profile (solid lines). The reactions are: C1 (black lines), C2 (red lines), C3 (green lines), C4 (blue lines), and C5 (cyan lines) (see Table 6)
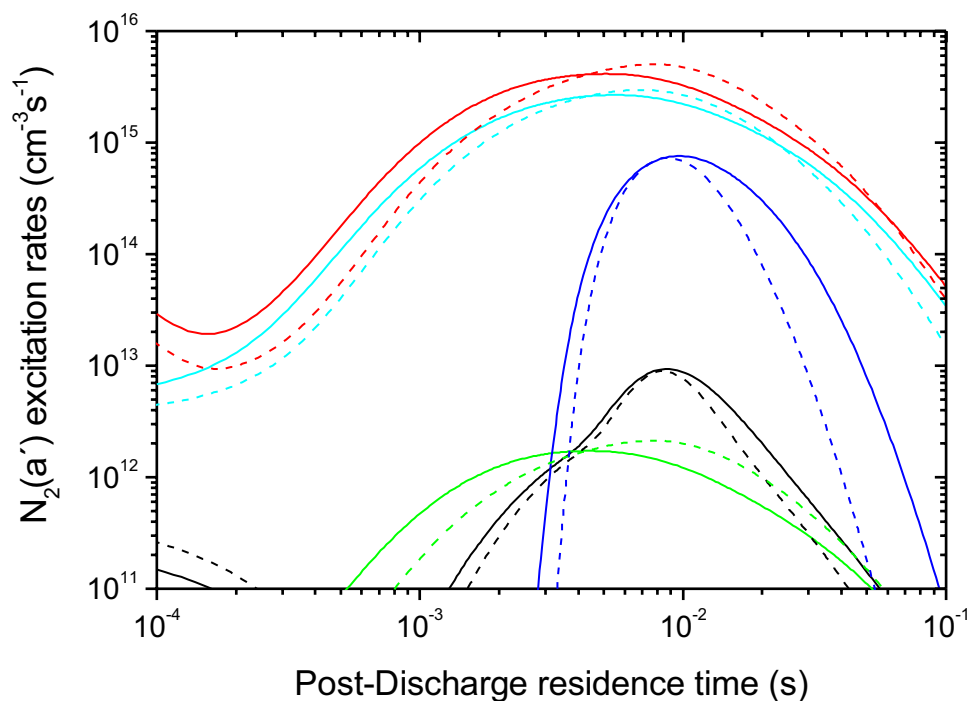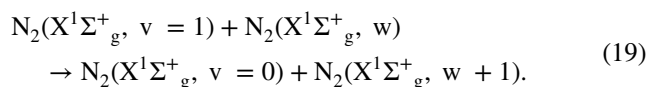
[24] whose rate constants are functions of the gas temperature parameter [15].

In order to conclude our analysis on the aspects concerning the two different approaches for the gas temperature in the PA kinetic modeling, we present the calculated VDFs for the studied discharge experimental condition (2). The VDFs for the discharge condition (1) are not shown here since the gas temperature assumptions effects are similar to those ones found for condition (2). The VDFs calculated for different post-discharge residence times are presented in Figure 13. It is demonstrated by our results that the calculated VDFs for the measured gas temperature approximation are more excited than those ones obtained for the constant gas temperature approximation. The first consequence of such result is the manifestation of the excitation rates maxima for the molecular states happening earlier in the post-discharge residence times when the measured gas temperature approach is considered in the calculations. This phenomenon is markedly seen in the reactions C2 and C5 related to the $N_2(a'^1\Sigma^-_u)$ excitation rates found in Figure 12, and also observed in the other molecular states (see Figures 10 and 11). As a result, the maxima of the molecular states densities also occur earlier in the post-discharge residence times when the measured gas temperature is considered in the calculations (see Figures 6, 7 and 8). Another aspect can be inferred by the VDFs behavior. As seen the VDFs obtained for the measured gas temperature are more excited after the maximum excitation is reached, which occurs at residence times on the order of 10^{-2} s. If we observe the calculated VDFs at t = 50 ms, the VDF for the measured gas temperature approach

is considerably more excited than that one for the constant gas temperature assumption. This behavior is in accordance with the excitation rates for the molecular states after their maxima occur, producing higher excitation rates at these residence times and resulting in a slower decrease of the molecules densities after the maximum densities are attained in the case of the measured gas temperature approximation.

As we have found more excited VDFs for the measured gas temperature methodology, this fact can be understood as a consequence of the higher vibrational quanta pumping in this situation. To gain an understanding on this phenomenon we have calculated the V-V rate constants for the discharge condition (2) considering the constant gas temperature of 420 K and the temperature variation from equation (18) as a function of the post-discharge residence time. The V-V rate constants $Q_{1,0}^{w,w+1}$ with $0 \leq w \leq 45$ for the V-V reactions [15] are shown in Figure 14:

$$
\begin{aligned}
N_2(X^1\Sigma^+_g, \; v = 1) &+ N_2(X^1\Sigma^+_g, \; w) \\
&\rightarrow N_2(X^1\Sigma^+_g, \; v = 0) + N_2(X^1\Sigma^+_g, \; w + 1).
\end{aligned}
\tag{19}
$$

These reactions are representative for the vibrational quanta pumping mechanism in the post-discharge. As observed in the figure, the rate constants present higher values for post-discharge residence times shorter than 10 ms as compared to the rate constants calculated for the fixed gas temperature of 420 K. At 10 ms, the rate constants for the fixed gas temperature and the measured gas temperature approximation are very close. This fact corroborates to a faster vibrational quanta pumping in this time interval,

Fig. 13 $N_2(X^1\Sigma^+_g)$ calculated VDFs for discharge condition (2). The solid lines are the calculations for the measured gas temperature T2(t) (see Eq. (18)). The dashed lines are the calculations for a constant gas temperature of 420 K. The post-discharge residence times are: 10^{-4} s (black lines), 10^{-3} s (red lines), 10^{-2} s (green lines), and 5×10^{-2} s (blue lines)
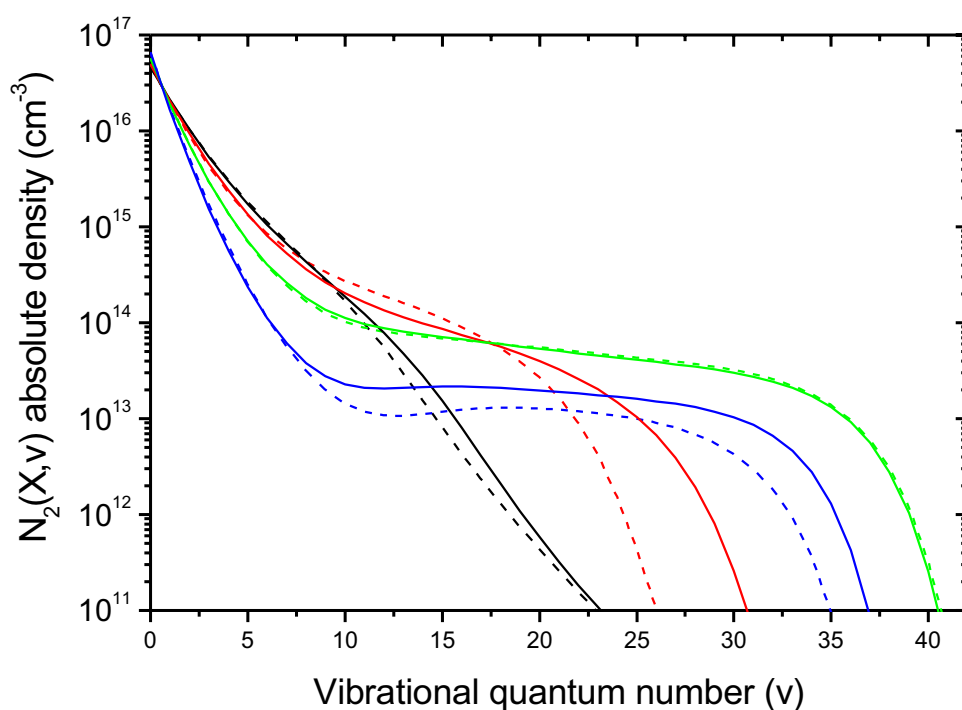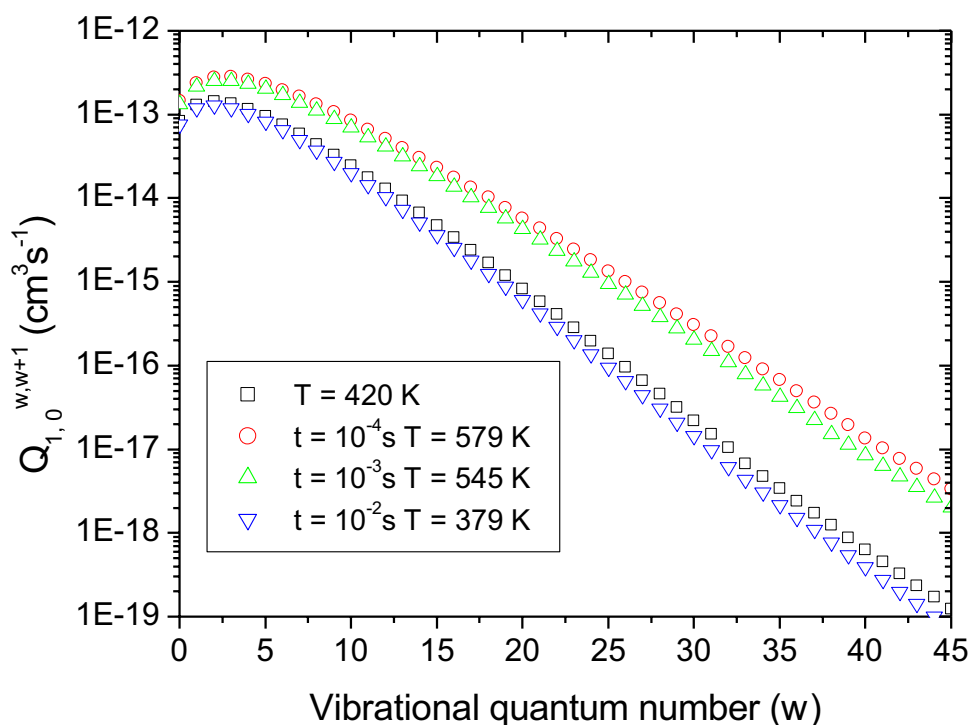
Fig. 14 Vibrational-vibrational (V-V) $Q_{1,0}^{w,w+1}$ rate constants calculated for discharge condition (2). The rate constants are calculated for a constant gas temperature of 420 K and as functions of Eq. (18) for some post-discharge residence times. The curves are specified in the figure legend

resulting in more excited VDFs for the measured gas temperature approach. We should also note that V-V rate constants are more efficient in reactions involving low lying vibrational levels.

We also analyze the V-T processes occurring in the post-discharge. The kinetic model accounts for V-T processes between the excited vibrational states and nitrogen molecules and atoms. In between the V-T processes involving nitrogen atoms, we consider the V-T mono-quantum deactivation

Fig. 15 $N_2(X^1\Sigma_g^+, v)$—$N(^4S)$ multi-quantum V-T rate constants for discharge condition (2), at a fixed gas temperature of 420 K and with the gas temperature following Eq. (18)
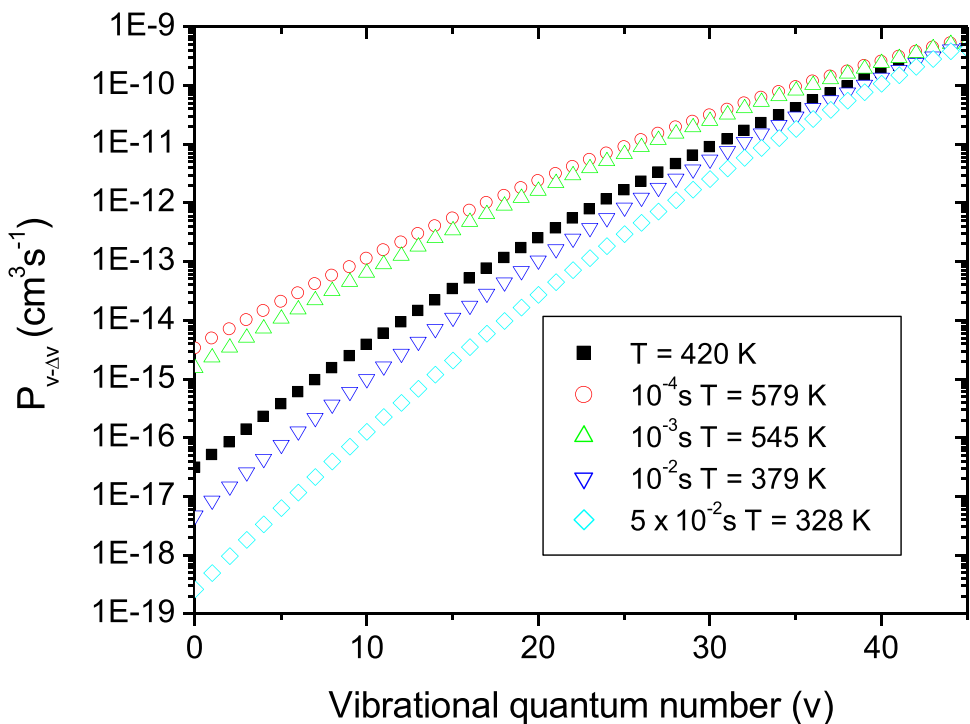
processes and multi-quantum deactivation processes [15]. The last ones are the most efficient in the deactivation of vibrational states. We calculated the rate constants of these reactions for a constant gas temperature of 420 K and also for the variation of the gas temperature following equation (18). The rate constants are presented in Figure 15. An important feature of the V-T processes is that they are efficient for the high vibrational states as can be seen in the figure. A consequence of this fact is the dominant role of the V-V processes in times ranging from the beginning of the post-discharge up to times on the order of 10 ms. In such times range the high vibrational levels are low populated (see Figure 13) and the V-V reactions dominate the VDF behavior, pumping energy from the low to the intermediate and high vibrational levels. At 10 ms, a density plateau is developed with the V-T processes becoming more important due the relevant density of high vibrational levels. We can observe for times on the order of 50 ms (blue curves in Figure 13) that vibrational deactivation is more pronounced in the fixed gas temperature approximation. Inspection of Figure 15 shows that V-T rate constants of $N_2(X^1\Sigma^+_g, v)$ - $N(^4S)$ collisions are greater for the fixed gas temperature approximation with respect to the rate constants for $t = 50$ ms, causing a more pronounced depletion of the highly excited vibrational levels.

4 Conclusion

We studied the effects of considering a post-discharge representative constant gas temperature and the measured gas temperature variation along the post-discharge on the kinetic modeling of the pink afterglow generated by flowing nitrogen DC discharges. Loureiro et al. [11] and Levaton et al. [15] have considered a representative value of 400 K for the gas temperature in the PA modeling of the flowing nitrogen microwave and direct current discharges. On the other hand, Sá et al.[13] have considered the measured gas temperature variation along the post-discharge in the PA modeling. These works have produced consistent results. Therefore, a question arises on how these different approximations affect the PA global kinetic modeling. The aim of our present study is to unveil the kinetics aspects of the PA modeling under such considerations. We calculated the $N_2(A^3\Sigma^+_u)$, $N_2(B^3\Pi_g)$, $N_2(a'^1\Sigma^-_u)$, $N_2^+(X^2\Sigma^+_g)$, $N_2^+(B^2\Sigma^+_u)$, N_3^+, and N_4^+ density profiles for the two gas temperature approaches. We observed that the species density profiles are very similar for these different methodologies. Focusing on the molecular triplet and singlet states, it was observed a global behavior where the maximum densities found in the PA are a few higher (5 to 32%) for the constant gas temperature approach, and also that the maximum densities occur at longer post-discharge residence times for this assumption (0 to 33%) (see Table 2 and 3). In order to deepen the analysis, we

calculated the excitation rates of these states. We determined the dominant excitation mechanisms and observed that the excitation rates for the constant gas temperature assumption also present higher maximum values occurring at later post-discharge residence times supporting the phenomena found for the density profiles. We also noted that the dominant excitation mechanisms do not depend on the gas temperature in their rate constants. This fact demonstrated that a global kinetic effect occurs for the different gas temperature approaches. Then, we analyzed the VDFs for the two cases. It was observed that the VDFs for the measured gas temperature approximation are more excited than those ones found for the constant gas temperature approach. This explains why the density maxima for the measured gas temperature approximation occur earlier than those ones for the constant gas temperature. Since all kinetic mechanisms of excitation, ionization, and dissociation in the PA depend directly or indirectly on the $N_2(X^1\Sigma^+_g, v)$ states, we have found the source of the excitation rates and species densities behaviors under the two assumptions. Finally, we calculated the V-V and V-T rate constants for the two assumptions. It was verified that V-V processes dominate the VDFs behavior in the earlier post-discharge residence times ($t < 10$ ms) and the V-T processes become important at longer residence times. The V-V and V-T rate constants dependence on the gas temperature explains the behavior found for the $N_2(X^1\Sigma^+_g)$ VDFs for the two different gas temperature approaches. As the main conclusion, considering the studied experimental conditions, it was shown that the constant gas temperature approximation produces reliable results in the PA kinetic modeling, being an acceptable approximation for 0-D kinetic studies of flowing nitrogen DC post-discharges, in the lack of measured gas temperature profiles.

Data Availability The data that support the findings of this study are avaiable upon reasonable request from the authors.

Declarations

References

1. H.H. Bromer, J. Hesse, Z. Physik **219**, 269 (1969)
2. V. Mazánková, D. Trunec, F. Krčma, J. Chem. Phys. **141**, 154307 (2014)
3. F. Krčma, M. Žáková, J. Phys. D Appl. Phys. **54**, 369 (2009)
4. P. Supiot, O. Dessaux, P. Goudmand, J. Phys. D Appl. Phys. **28**, 1826 (2009)

5. C. Foissac, A. Campargue, A. Kachanov, P. Supiot, G. Weirauch, N. Sadeghi, J. Phys. D Appl. Phys. **33**, 2434 (2000)

6. P. Supiot, D. Blois, S. De Benedictis, G. Dilecce, M. Barj, A. Chapput, O. Dessaux, P. Goudmand, J. Phys. D Appl. Phys. **32**, 1887 (1999)

7. J. Levaton, J. Amorim, D. Franco, J. Phys. D Appl. Phys. **38**, 2204 (2005)

8. J. Levaton, J. Amorim, Chem. Phys. **435**, 1 (2014)

9. J. Levaton, A.N. Klein, C. Binder, Plasma Chem. Plasma Process. **38**, 1259 (2018)

10. N.A. Popov, Plasma Phys. Rep. **35**, 436 (2009)

11. J. Loureiro, P.A. Sá, V. Guerra, J. Phys. D Appl. Phys. **34**, 1769 (2001)

12. J. Loureiro, P.A. Sá, V. Guerra, J. Phys. D Appl. Phys. **39**, 122 (2005)

13. P.A. Sá, V. Guerra, J. Loureiro, N. Sadeghi, J. Phys. D Appl. Phys. **37**, 221 (2003)

14. V. Guerra, P.A. Sá, J. Loureiro, J. Phys. Conf. Ser. **63**, 012007 (2007)

15. J. Levaton, J. Amorim, A.R. Souza, D. Franco, A. Ricard, J. Phys. D Appl. Phys. **35**, 689 (2002)

16. J. Levaton, J. Amorim, A. Ricard, J. Phys. D Appl. Phys. **45**, 505203 (2012)

17. J. Levaton, A.N. Klein, C. Binder, Phys. Plasmas **25**, 013531 (2018)

18. J. Levaton, A.N. Klein, J. Amorim, J.H.F. Severo, J. Phys. D Appl. Phys. **54**, 505205 (2021)

19. J. Amorim, IEEE Trans. Plasma Sci. **33**, 368 (2005)

20. A. Lofthus, P.H. Krupenie, J. Phys. Chem. Ref. Data **6**, 113 (1977)

21. L.G. Piper, J. Chem. Phys. **90**, 7087 (1989)

22. N.A. Gorbunov, N.B. Kolokolov, A.A. Kudryavtsev, Sov. Phys. Tech. Phys. **33**, 1104 (1988)

23. N.A. Gorbunov, N.B. Kolokolov, A.A. Kudryavtsev, D. Book, Sov. Phys. Tech. Phys. **36**, 616 (1991)

24. M. Capitelli, *Topics in Current Physics: Nonequilibrium Vibrational Kinetics* (Springer, Berlin, 1986), p.315

25. J. Levaton, A.N. Klein, J. Amorim, J.H.F. Severo, Plasmas Sources Sci. Technol. **31**, 125010 (2022)

26. N. Sadeghi, C. Foissac, P. Supiot, J. Phys. D Appl. Phys. **34**, 1779 (2001)

27. J. Levaton, A.N. Klein, J. Amorim, Phys. Plasmas **27**, 063503 (2020)

28. J. Levaton, J. Amorim, V. Monna, J. Nagai, A. Ricard, Eur. Phys. J. Appl. Phys. **26**, 59 (2004)

29. N. Britun, M. Gaillard, A. Ricard, Y.M. Kim, K.S. Kim, J.G. Han, J. Phys. D Appl. Phys. **40**, 1022 (2007)

30. L. Hochard, L. Magne, G. Cernogora, J. Peeters, 12th ESCAMPIG (Noordwijkerhout, The Netherlands) **18E**, 336 (1994)

31. V. Guerra, J. Loureiro, Plasmas Sources Sci. Technol. **6**, 361 (1997)

32. J. Levaton, J. Amorim, Chem. Phys. **397**, 9 (2012)

33. A.A. Matveyev, V.P. Silakov, Plasmas Sources Sci. Technol. **8**, 162 (1999)

34. L.G. Piper, J. Chem. Phys. **88**, 6911 (1988)

35. L.G. Piper, J. Chem. Phys. **87**, 1625 (1987)

36. B. Gordiets, C.M. Ferreira, M.J. Pinheiro, A. Ricard, Plasmas Sources Sci. Technol. **7**, 363 (1998)

37. L. Magne, G. Cenorgora, P. Veis, J. Phys. D Appl. Phys. **25**, 472 (1992)

38. R.S. Freund, J. Chem. Phys. **56**, 4344 (1972)

39. V. Guerra, P.A. Sá, J. Loureiro, Plasmas Sources Sci. Technol. **12**, S8 (2003)